

Article

Analytical Modeling, Analysis and Diagnosis of External Rotor PMSM with Stator Winding Unbalance Fault

Ahmed Belkhadir ^{1,2}, Remus Pusca ¹, Driss Belkhayat ², Raphaël Romary ^{1,*} and Youssef Zidani ²

¹ Univ. Artois, UR 4025, Laboratoire Systèmes Electrotechniques et Environnement (LSEE), F-62400 Béthune, France

² Univ. Cadi Ayyad, P.O. Box 549, Laboratoire des Systèmes Electriques, Efficacité Energétique et Télécommunications (LSEET), Faculty of Sciences and Technologies, Marrakech 40000, Morocco

* Correspondence: raphael.romary@univ-artois.fr

Abstract: Multiple factors and consequences may lead to a stator winding fault in an external rotor permanent magnet synchronous motor that can unleash a complete system shutdown and impair performance and motor reliability. This type of fault causes disturbances in operation if it is not recognized and detected in time, since it might lead to catastrophic consequences. In particular, an external rotor permanent magnet synchronous motor has disadvantages in terms of fault tolerance. Consequently, the distribution of the air-gap flux density will no longer be uniform, producing fault harmonics. However, a crucial step of diagnosis and controlling the system condition is to develop an accurate model of the machine with a lack of turns in the stator winding. This paper presents an analytical model of the stator winding unbalance fault represented by lack of turns. Here, mathematical approaches are used by introducing a stator winding parameter for the analytical modeling of the faulty machine. This model can be employed to determine the various quantities of the machine under different fault levels, including the magnetomotive force, the flux density in the air-gap, the flux generated by the stator winding, the stator inductances, and the electromagnetic torque. On this basis, a corresponding link between the fault level and its signature is established. The feasibility and efficiency of the analytical approach are validated by finite element analysis and experimental implementation.

Keywords: stator winding unbalance fault; external rotor permanent magnet synchronous motor; fault harmonics; diagnosis; lack of turns; analytical approach; finite element analysis



Citation: Belkhadir, A.; Pusca, R.; Belkhayat, D.; Romary, R.; Zidani, Y. Analytical Modeling, Analysis and Diagnosis of External Rotor PMSM with Stator Winding Unbalance Fault. *Energies* **2023**, *16*, 3198. <https://doi.org/10.3390/en16073198>

Academic Editors: Moussa Boukhniher and Larbi Djilali

Received: 3 March 2023

Revised: 25 March 2023

Accepted: 28 March 2023

Published: 1 April 2023



Copyright: © 2023 by the authors. Licensee MDPI, Basel, Switzerland. This article is an open access article distributed under the terms and conditions of the Creative Commons Attribution (CC BY) license (<https://creativecommons.org/licenses/by/4.0/>).

1. Introduction

In recent years, external rotor permanent magnet synchronous motors (ER-PMSMs) mounted directly in the wheels of vehicles has been one of the trends in drive systems employed in hybrid and electrical vehicle (HEV) powertrains. The design of this type of motor presents a challenge, as it must be characterized by high durability and energy efficiency [1–3].

Interest in continually developing techniques for the diagnosis of faults in electrical machines is related to several factors. Firstly, the overall number of embedded motors that are employed in different applications, such as industrial systems, renewable energy generating systems, and HEVs [4]. However, owing to the ageing of materials, manufacturing faults, or severe conditions, various types of electrical, mechanical, and magnetic faults can occur in the machine [5], for example: open phase faults, interturn short circuit faults, lack of turns (LTs) faults in the stator winding, eccentricity, demagnetization, and magnetic circuit faults [6]. Hence, the integration of detection strategies, diagnosis, and fault-tolerant control becomes unavoidable. Moreover, during the real operation of the ER-PMSM, LTs faults may emerge due to manufacturing tolerances or ageing issues. Therefore, once the LTs fault appears, the stator current increases to generate enough torque, which leads to

torque and speed ripples, and further exacerbates thermal problems. As a result, early diagnosis of the LTs fault is critical for preventing deterioration of ER-PMSM performance and reducing eventual losses by implementing the most effective corrective measures. These measures may consist of repairing the faulty machine or, in certain situations, appropriately reconfiguring the control strategy [6].

Currently, several studies have been conducted on the diagnosis and localization of stator winding faults in ER-PMSMs. Modeling and experiments have been used as the first step in these studies, and research aims to extract electrical signals and quantities such as voltage and currents, mechanical quantities such as speed, torque and vibration, and magnetic field signals such as magnetic flux and density [7–9]. Secondly, appropriate signal processing methods were employed to extract fault characteristics from various signals, identify the mode, assess the severity, and classify the fault [10,11].

The lack of turns (LTs) faults can be detected via different approaches based on signals, data, and models. The first technique aims to identify characteristic fault frequencies in measured ER-PMSM signals [12,13], which are processed using time-frequency signal analysis tools, such as the Fourier transform [14,15], wavelet transforms [16], and the Hilbert–Huang transform [17]. Unlike the Fourier transform, the drawback of wavelets and Hilbert–Huang transforms is their incompatibility with real-time analysis. Additionally, a detection technique using an analysis of the external field, provided by sensors positioned around the machine, using information fusion methods is proposed in [18–21], but these methods require an accurate knowledge of the external stray flux.

Advanced machine learning methods are also employed to detect ER-PMSM stator faults. These methods are attractive due to their advanced data processing capabilities combined with external machine signals, such as vibration, acoustic noise, and torque [22]. A one-dimensional convolutional neural network model, which analyzes torque and current signals to diagnose the motor across a wide range of speeds, variable loads, and fault levels, is proposed in [23]. These kinds of advanced algorithms are very efficient, but they require a large amount of computation and historical data to form models and classify localized defects, as well as extremely high hardware requirements.

This research focuses on the diagnosis of LTs faults in ER-PMSMs by examining and analyzing the current and speed spectrum, allowing a simple and powerful implementation of an online fault diagnosis approach. To better understand the influence and consequences of the fault, an analytical approach and finite element model validation were employed. The finite element analysis (FEA) offers the benefits of a well-established application and high computational precision and accuracy. The analytical approach involves the development of a mathematical model that replicates the behavior of the machine in the presence of the fault. This model can be used to predict the impact of the fault on various machine quantities, and can contribute to the development of effective fault diagnosis methods. Overall, the combination of the analytical approach and FEA validation provides comprehensive knowledge of the impact of the LTs fault on ER-PMSMs employed in electric mobility.

The main contributions of this research are as follows: a novel technique and approach for modeling LTs faults in ER-PMSMs. The suggested analytical model requires less computational time and can subsequently provide an accurate reference for real-time fault diagnosis, accuracy, and maintenance. Then, the experimental validation for an ER-PMSM operating in the case of a motor is presented. Experimental measurements that must be taken to ensure a reliable diagnosis are also presented.

The main structure of this paper is as follows: in Section 2, the healthy and faulty analytical models are established to examine how the LTs fault impacts the various electrical and mechanical quantities of the machine, and the FEA is used to verify the effectiveness and accuracy of the proposed analytical model. The experimental setup is provided in Section 3, and the experimental results are in Section 4. Finally, Section 5 summarizes the conclusions and prospects of the presented work.

2. Exhaustive Analysis of LTs Fault

After evoking the secondary consequences at the origin of the stator winding unbalance fault illustrated by LTs, this section aims to provide a global comprehension of the machine in healthy and faulty conditions using an analytical approach and numerical validation.

The development of a mathematical model enabling simulation of the behavior of the ER-PMSM in the two healthy and faulty operating modes is indicated below. This model is based on a 2D extension of the winding function approach to determine the different inductances of the machine, taking into consideration all the space harmonics, the real geometry of the ER-PMSM, as well as the distribution of the windings in the stator slots. The model of the 24 slots and 22 poles of the ER-PMSM with concentric winding is shown in Figure 1. The major specifications of the machine are listed in Table 1.

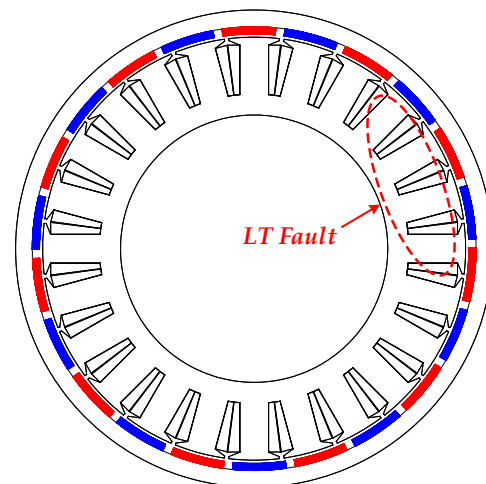


Figure 1. The model of the double-layer fractional-slot concentrated-wound ER-PMSM.

Table 1. ER-PMSM parameters.

Parameter	Symbol	Value	Parameter	Symbol	Value
Rated power (kW)	P	1.5	Inner rotor diameter (mm)	–	183
Rated speed (rpm)	w	600	Length (mm)	L_{axe}	35
DC bus voltage (V)	V_{DC}	150	Air-gap length (mm)	g	1.365
Rated current (A_{RMS})	I_N	11	Stator slot width (mm)	l_e^s	10.37
Rated torque (Nm)	Γ_e	24	Stator tooth width (mm)	l_d^s	21.1431
Number of poles	p	22	Stator fictive slot depth (mm)	p^s	2.0740
Number of phases	m	3	Slot opening width (mm)		2
Number of slots	N^s	24	Magnet thickness (mm)	h_m	3
Number of turns per coil	N_T	22	Residual flux density of PM (T)	B_r	1.26
Outer stator diameter (mm)	–	112	Magnet-arc to pole-pitch ratio (%)	α_p	85.55
Inner stator radius (mm)	R_s	88.6350	Permanent magnets	–	NdFeB N38SH
Outer rotor diameter (mm)	–	186	Magnetic steel	–	M530-50A

The analytical model is developed based on the assumptions given throughout this section, as follow [24]:

- (1) Magnetic saturation is negligible;
- (2) Ideal ferromagnetic steel and the magnetic energy is concentrated in the air-gap;
- (3) Small air-gap relative to the internal diameter of the stator and radial magnetic field (tangential magnetic fields are negligible);
- (4) Neglected conductivity and eddy current effects.

2.1. Analytical Approach

2.1.1. Distribution Function of the ER-PMSM

The distribution function of a coil placed in the magnetic circuit delivers information about its position. Therefore, the objective is to apply the winding function approach to compute the inductances of the 24 slots and 22 poles of a double-layer fractional-slot concentrated-wound (FSCW) ER-PMSM (24/22) [24]. Their waveforms are shown in Figure 2.

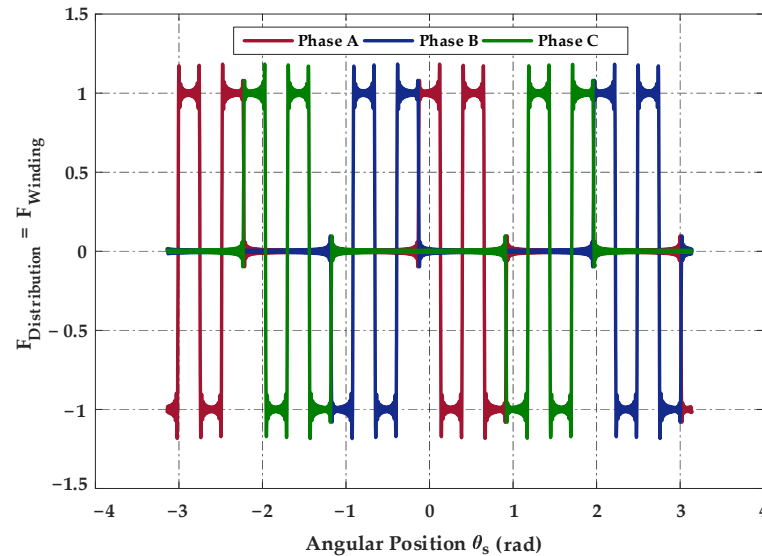


Figure 2. Distribution function of ER-PMSM.

The Fourier decomposition of the distribution function can be given by:

$$F_{distribution} = \frac{P_e}{2\pi} O_c + \frac{2}{\pi} \sum_{h=1}^{+\infty} \frac{1}{h} \sin\left(hP_e \frac{O_c}{2}\right) \cos(hP_e \theta_s) \quad (1)$$

The total distribution function of a winding is the sum of the distribution functions of a winding, and the sum of the distribution functions of the coils in a series of the same phase per pair of poles of this winding.

$$F_{distribution,T}(\theta_s) = \sum_{i=1}^q F_{distribution}(\theta_s) \quad (2)$$

where P_e is the winding periodicity, O_c is the coil opening angle, q is the coil number, and θ_s is the angular position in relation to the stator reference axis.

2.1.2. Winding Function of the ER-PMSM

The winding function presents the magnetomotive force (MMF) of a single-turn winding carrying a unit current. We may represent these functions as a series of harmonics due to the winding's periodicity and each phase coil's function, which contains periodic square pulses. In this analysis instance, the mean value of the distribution function is null. However, Figure 2 illustrates the winding function, which is proportional to the distribution function.

$$F_w(\theta_s) = F_{distribution,T}(\theta_s) - \langle F_{distribution,T}(\theta_s) \rangle \quad (3)$$

The spatial harmonic amplitudes of the winding function, obtained from Equation (3), for a stator with concentrated winding around a double-layer tooth is illustrated in Figure 3.

Evidently, the harmonic of rank $h = 11$ had the highest amplitude of 0.4396 for a machine (24/22).

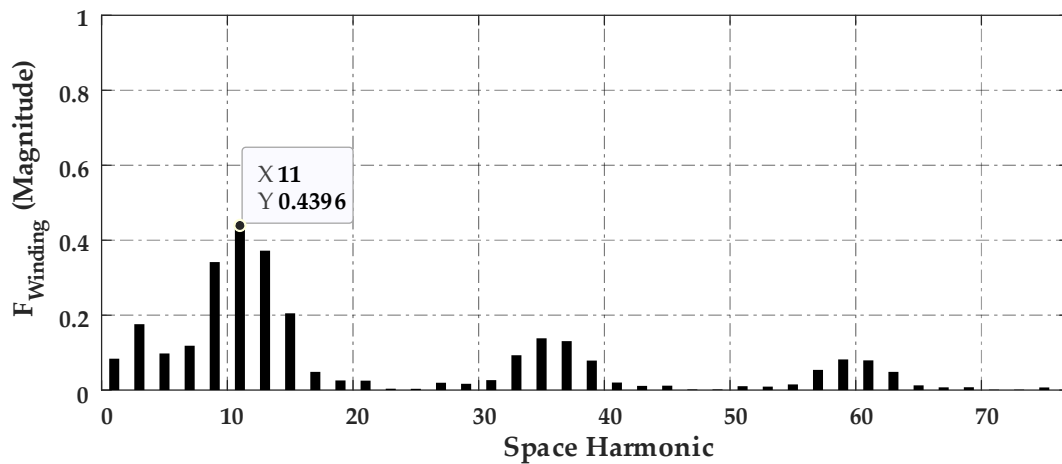


Figure 3. Harmonic spectrum of the winding function.

2.1.3. Winding Factor of the ER-PMSM

The winding factor presents the efficiency of the coil arrangement to create a MMF and determines the capacity of the electromagnetic torque production. We can write a general presentation of the total winding factor K_w of harmonic h , using the voltage phasor diagram [25]:

$$K_w = K_d K_p \quad (4)$$

where K_d is the distribution factor, K_p is the pitch factor, $\alpha_u = p \frac{2\pi}{Q}$ is the slot angle, m is the number of phases, $Q = 2qpm$ is the number of slots, $\tau_p = \frac{\pi D}{2p}$ is the pole pitch, and D is the diameter of the air-gap.

$$K_d = \frac{\sin\left(h \frac{q\alpha_u}{2}\right)}{q \sin\left(h \frac{\alpha_u}{2}\right)} = \frac{\sin\left(h \frac{Q}{2pm} \frac{2\pi p}{2Q}\right)}{q \sin\left(h \frac{2\pi p}{2q2pm}\right)} = \frac{\sin\left(h \frac{\pi}{6}\right)}{q \sin\left(h \frac{\pi}{6q}\right)} \quad (5)$$

$$K_p = \sin\left(h \frac{O_c}{\tau_p} \frac{\pi}{2}\right) \quad (6)$$

According to Figure 4, the spectrum represents the spatial distribution of the winding factor. The maximum torque of the machine generated in the air-gap will be created by the $h11$ component, with a winding factor of 0.949. This component corresponds to the fundamental, with a rank $h = p$.

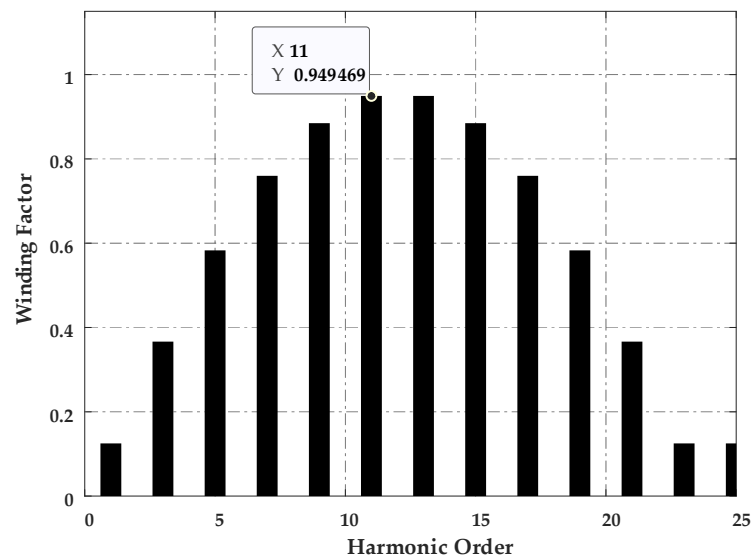


Figure 4. Harmonic spectrum of the winding factor.

2.1.4. Magnetomotive Force (MMF)

A. Healthy MMF of the ER-PMSM

The MMF of a double-layer FSCW stator is rich in harmonics. However, this harmonic content leads to torque ripples, unbalanced saturation, and iron losses [26,27]. For this reason, the combination of slots and number of poles has specific features that must be examined and studied before that the machine is designed. The harmonics of the winding factor (Figure 4) are frequently employed as an indication of the properties of this combination [28].

The spatial MMF distribution of a phase winding is obtained by superimposing the MMF of all its coils. Due to the periodicity of the winding, the healthy MMF of each phase j includes periodic square pulses, and can be represented by a Fourier series decomposition, as follows:

$$\varepsilon_j^s(t, \theta_s) = K_w N_T i_j^s(t) F_w(\theta_s) \quad (7)$$

where N_T is the turns number and $i_j^s(t) = \sqrt{2} I_j^s \sin(\omega t + \varphi_j)$ is the temporal expression of sinusoidal current.

The total healthy MMF generated by the 22 pole, 24 slot FSCW stator is determined using the following formula:

$$\varepsilon^s(t, \theta_s) = \sum_{j=1}^m (\varepsilon_j^s(t, \theta_s)) \quad (8)$$

$$\varepsilon^s(t, \theta_s) = \frac{1}{\pi} m I_{\max} N_T \sum_{h=1}^{+\infty} \frac{1}{h} K_w \sin\left(h P_e \frac{O_c}{2}\right) \cos(h P_e \theta_s - (\omega t - \varphi)) \quad (9)$$

The distribution of the total healthy MMF of the three-phase stator winding is shown in Figure 5 when it is supplied with a balanced three-phase current of $f = 110$ Hz. The harmonic spectrum of the total MMF distribution in the healthy case is determined from Equations (8) and (9), and illustrated in Figure 6. We notice that the harmonic of rank $h11$ is the most dominating of ER-PMSM (24/22).

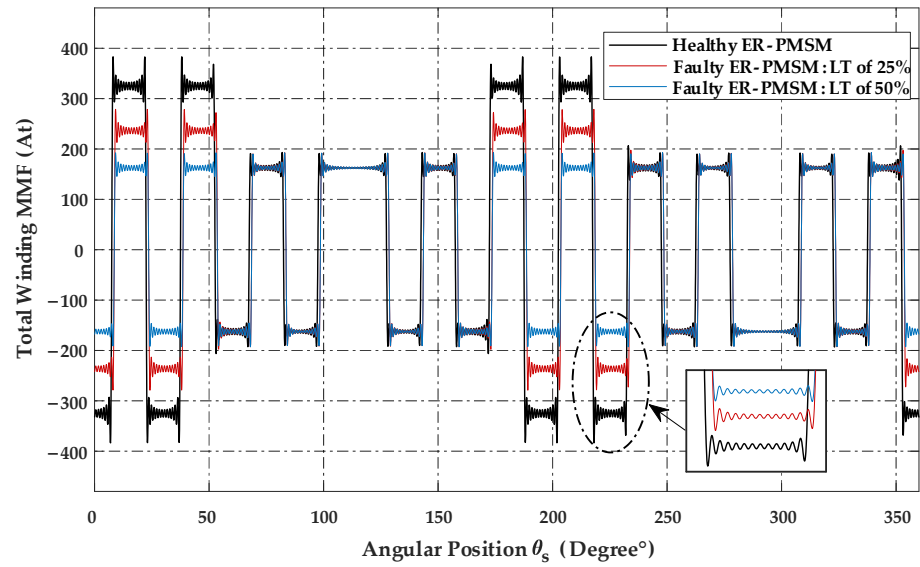


Figure 5. Healthy and faulty stator MMF distribution.

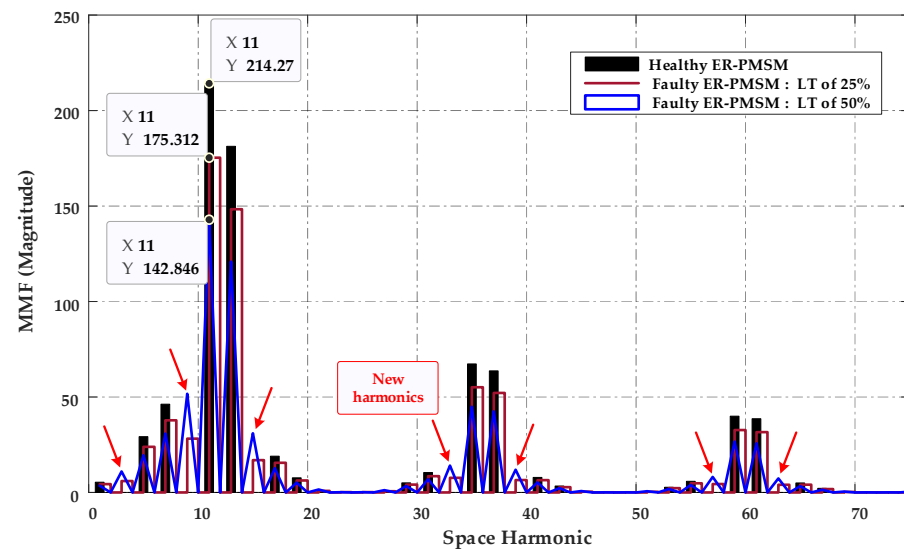


Figure 6. Spatial harmonic spectrum of the total healthy and faulty MMF.

B. Faulty MMF of the ER-PMSM

When a stator winding unbalanced fault of LTs occurs in the machine, the stator MMF will be impacted by the fault. The general analytic model of the faulty MMF is obtained using the previously stated methodologies and is shown in Figure 5, which can be represented by the following expressions:

$$\varepsilon_{j,faulty}^s(t, \theta_s) = K_w F_{w,faulty}(\theta_s) N_T i_j^s(t) \quad (10)$$

$$F_{w,faulty}(\theta_s) = \frac{N_f}{N_T} F_{w,a}(\theta_s) + F_{w,b}(\theta_s) \cos\left(\omega t - \frac{2\pi}{3}\right) + F_{w,c}(\theta_s) \cos\left(\omega t + \frac{2\pi}{3}\right) \quad (11)$$

$$\varepsilon_{faulty}^s(t, \theta_s) = \sum_{j=1}^{+\infty} \varepsilon_{j,faulty}^s(t, \theta_s) \quad (12)$$

The analytical modeling in the faulty state is performed for two fault levels: 25% and 50% LTs in phase A.

Where $F_{w, faulty}$ is the winding function in the faulty state, and N_f is the number of faulty stator turns.

A comparison between the harmonic content of the MMF is presented in Figure 6. Evidently, when the machine is subjected to the LTs fault, all of the odd harmonics are present in the spectrum, as well as the appearance of new harmonics that are due to the LTs fault levels (Red arrows).

2.1.5. Air-Gap Flux Density

The permeance function is proportional to the inverse of the air-gap thickness, and depends only on the average permeance of the air-gap and the form of the stator slots.

For determination of the air-gap permeance, a simplified geometry of the motor shown in Figure 7 is considered, with a fictitious model for the slots resulting from the assumptions for a nonsalient FSCW ER-PMSM, and with radial field lines.

$$\varphi(\theta_s) = P_0 + \sum_{K_s=1}^{+\infty} P_{K_s} \cos(K_s N^s \theta_s) \tag{13}$$

$$P_0 = \frac{\mu_0}{g + p^s} \left(1 + \frac{p^s r_d^s}{g} \right) \tag{14}$$

$$P_{K_s} = 2\mu_0 \frac{p^s}{g(g + p^s)} \frac{\sin(K_s r_d^s \pi)}{K_s \pi} \tag{15}$$

where $\mu_0 = 4\pi 10^{-7}$ is the permeability of a vacuum approximately equal to that of the air, $p^s = l_e^s/5$ is the stator fictive slot depth [18], r_d^s is the stator toothing ratio, and K_s is the permeance rank.

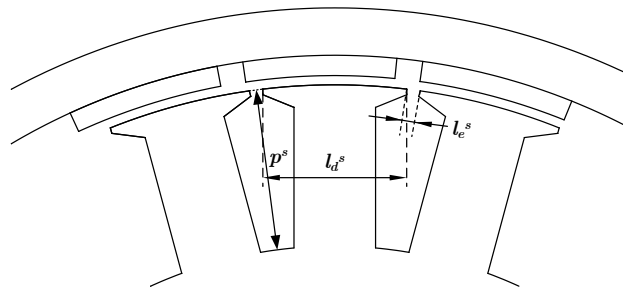


Figure 7. Geometry adopted for the stator slots of the ER-PMSM.

The healthy and faulty air-gap flux density for a sinusoidal current system can be written as the following expression:

$$b^s(t, \theta_s) = \varphi(\theta_s) \varepsilon^s(t, \theta_s) \tag{16}$$

$$b_{faulty}^s(t, \theta_s) = \varphi(\theta_s) \varepsilon_{faulty}^s(t, \theta_s) \tag{17}$$

Here, it is assumed that the magnetic field distribution would be affected in the fault condition. Depending on the two levels of the LTs fault, there is a reduction in the flux inside the stator core. Based on Figure 9, the magnitude of the flux density is considerably impacted by the fault. The spectrum of the flux density harmonic in the air-gap is depicted in Figure 10. The amplitude of the fundamental component in the healthy condition and no-load case is 0.0652 T.

2.1.6. Inductances in Healthy and Faulty FSCW ER-PMSMs

To be able to determine the different parameters of the machine in healthy and damaged modes for examining the structure of the ER-PMSM, it is crucial to calculate the

values of the self and mutual inductances. In order to examine several configurations, these calculations are performed using an analytical approach, as well as a numerical and experimental validation model.

Inductances have a crucial role in this modeling technique since they account for the many effects that might occur in the machine. Accurate modeling will lead to additional information of the signals, and a good compromise in terms of model accuracy.

The inductances of the machine will be determined analytically using the previously stated winding function.

A. Healthy Magnetic Flux

The magnetic flux produced by a phase i flowing through a phase j winding is provided by the following equations:

$$\Phi_{ji,h}(t) = N_T \iint b_i^s(t, \theta_s) ds_j \quad (18)$$

$$\Phi_{ji,h}(t) = (N_T)^2 I_i(t) R_s L_{axe} K_w \int_0^{2\pi} F_{distribution,j}(\theta_s) \varphi(\theta_s) F_{w,i}(\theta_s) d\theta_s \quad (19)$$

The self-magnetic flux of phase A is given by:

$$\Phi_{aa,h}(t) = \frac{2}{P_e} R_s L_{axe} (N_T)^2 \frac{2I_{max}}{\pi} \varphi(\theta_s) \sum_{h=1}^{+\infty} \left[\frac{1}{h^2} K_w \sin^2 \left(h P_e \frac{O_c}{2} \right) \cos(\omega t - \varphi) \right] \quad (20)$$

The mutual magnetic flux between phase A and phase B can be expressed by:

$$\begin{aligned} \Phi_{ab,h}(t) &= \frac{2}{P_e} R_s L_{axe} (N_T)^2 \frac{2I_{max}}{\pi} \varphi(\theta_s) \\ &\sum_{h=1}^{+\infty} \left[\frac{1}{h^2} K_w \sin \left(h P_e \frac{O_c}{2} \right) \left(\sin \left(h P_e \frac{3O_c}{2} \right) - \sin \left(h P_e \frac{O_c}{2} \right) \right) \cos(\omega t - \varphi) \right] \end{aligned} \quad (21)$$

where R_s is the inner stator radius.

B. Faulty Magnetic Flux

The self-magnetic flux of phase A in the faulty state is given by:

$$\Phi_{a11,faulty}(t) = \frac{2}{P_e} R_s L_{axe} (N_f)^2 \frac{2I_{max}}{\pi} \varphi(\theta_s) \sum_{h=1}^{+\infty} \left[\frac{1}{h^2} K_w \sin^2 \left(h P_e \frac{O_c}{2} \right) \cos(\omega t - \varphi) \right] \quad (22)$$

$$\begin{aligned} \Phi_{a12,faulty}(t) &= -\frac{1}{P_e} R_s L_{axe} (N_f)^2 \frac{2I_{max}}{\pi} \varphi(\theta_s) \\ &\sum_{h=1}^{+\infty} \left[\frac{1}{h^2} K_w \sin \left(h P_e \frac{O_c}{2} \right) \left(\sin \left(h P_e \frac{3O_c}{2} \right) - \sin \left(h P_e \frac{O_c}{2} \right) \right) \cos(\omega t - \varphi) \right] \end{aligned} \quad (23)$$

The total flux linkage of a phase winding is the sum of the aforementioned, as follows:

$$\Phi_{a,faulty}(t) = \sum_{n=1}^8 \Phi_{an,faulty}(t) \quad (24)$$

A faulty mutual magnetic flux between phase A and phase b is given by:

$$\begin{aligned} \Phi_{a1b8,faulty}(t) &= \frac{1}{P_e} R_s L_{axe} N_T N_f \frac{2I_{max}}{\pi} \varphi(\theta_s) \\ &\sum_{h=1}^{+\infty} \left[\frac{1}{h^2} K_w \sin \left(h P_e \frac{O_c}{2} \right) \left(\sin \left(h P_e \frac{3O_c}{2} \right) - \sin \left(h P_e \frac{O_c}{2} \right) \right) \cos(\omega t - \varphi) \right] \end{aligned} \quad (25)$$

$$\begin{aligned} \Phi_{a5b4,faulty}(t) &= \frac{1}{P_e} R_s L_{axe} N_T N_f \frac{2I_{max}}{\pi} \varphi(\theta_s) \\ &\sum_{h=1}^{+\infty} \left[\frac{1}{h^2} K_w \sin \left(h P_e \frac{O_c}{2} \right) \left(\sin \left(h P_e \frac{3O_c}{2} \right) - \sin \left(h P_e \frac{O_c}{2} \right) \right) \cos(\omega t - \varphi) \right] \end{aligned} \quad (26)$$

$$\Phi_{ab,faulty}(t) = \Phi_{a1b8,faulty}(t) + \Phi_{a5b4,faulty}(t) \quad (27)$$

Figure 11 depicts the magnetic flux produced by the three phases with a fault of 25% and 50% of LTs of phase A.

C. Inductances in Healthy and Faulty States

The ER-PMSM inductances are calculated using the approach provided in [25,29], which uses the winding function corresponding to the MMF produced by the stator winding. Accordingly, the self or mutual inductances are determined from the following relation:

$$L_{ji,h} = (N_T)^2 R_s L_{axe} K_w \int_0^{2\pi} F_{distribution,j}(\theta_s) \varphi(\theta_s) F_{w,i}(\theta_s) d\theta_s \quad (28)$$

According to the analytical modeling of the faulty magnetic flux proposed and calculated from Equations (25) and (28), the general form of the faulty self and mutual inductance can be expressed as follows:

$$L_{a-A25\%/50\%} = \frac{\Phi_{a,faulty}(t)}{I_a(t)}; \quad M_{a-A25\%/50\%-b} = \frac{\Phi_{ab,faulty}(t)}{I_a(t)} \quad (29)$$

where the faulty inductances depend on the severity of the LTs fault, and the number of faulty stator turns N_f . The analytical calculation of self and mutual inductances is conducted as an example to explain the complete procedure. The other inductances can be derived similarly. Figure 12a–c exhibit, respectively, the healthy and faulty inductances according to the two LTs fault levels. All of the results obtained for healthy and degraded operations by the analytical and numerical approaches are close.

An AC immobilization test is employed for the experimental measurement (Figure 12). In this method, an AC current flows in phase A, while the other two phases are in an open circuit. The self-inductance is then obtained using the RMS voltage and current measured at different rotor positions [30].

2.2. Numerical Validation: Finite Element Analysis

In order to evaluate and validate the analytical approach, a two-dimensional FEA-2D model of the motor is tested and simulated (Figure 1). The analysis of the behavior for the LTs fault, with consideration of the electrical and mechanical quantities of the machine in operational mode, is performed in an open-loop system. All of the testing and analysis will be focused on the intrinsic features of the LTs fault. The main structural parameters and specifications are listed in Table 1. Figure 8 illustrates the study ER-PMSM machine with faulted turns and the mesh of the FEA model.

The impact of the LTs fault is at first examined without the influence of the controllers under two fault severities. The ER-PMSM with 24 slots and 22 poles is used for the fault analysis. The following analyses are performed at a level of 25% and 50% of LTs in phase A of the machine.

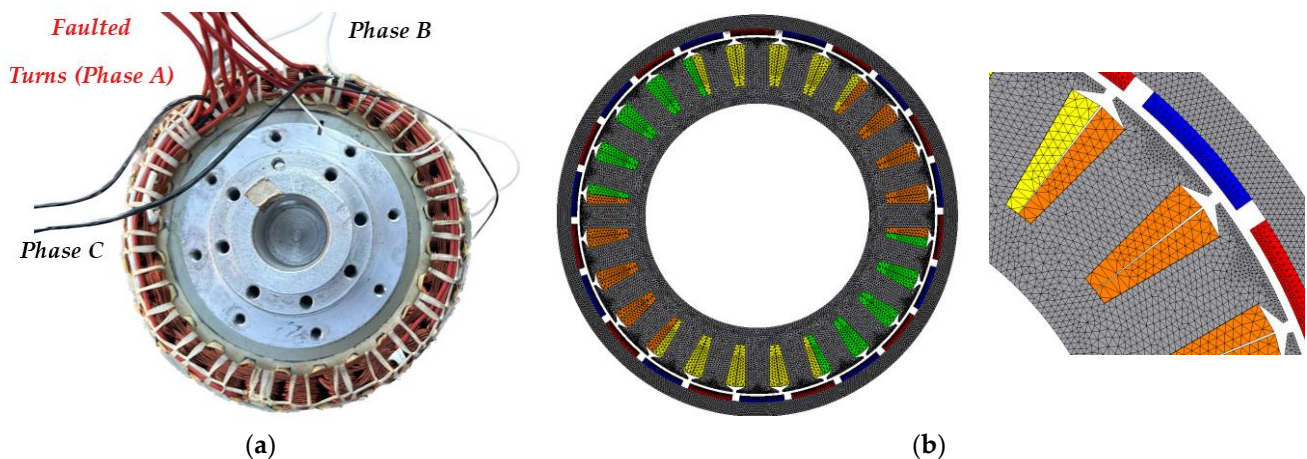


Figure 8. ER-PMSM with LTs in phase A. (a) ER-PMSM stator winding with LTs fault in phase A; (b) the mesh of the ER-PMSM FEA analysis.

Performance Analysis of ER-PMSM with LTs Fault

Figure 9 illustrates the radial air-gap flux density at no load obtained by the analytical model and the FEA model in the healthy and faulty states according to the two LT fault levels. In the case of an unbalanced stator winding fault, the amplitudes of the no-load flux density waveforms drop. However, all analyses are consistent with the analytical analyses.

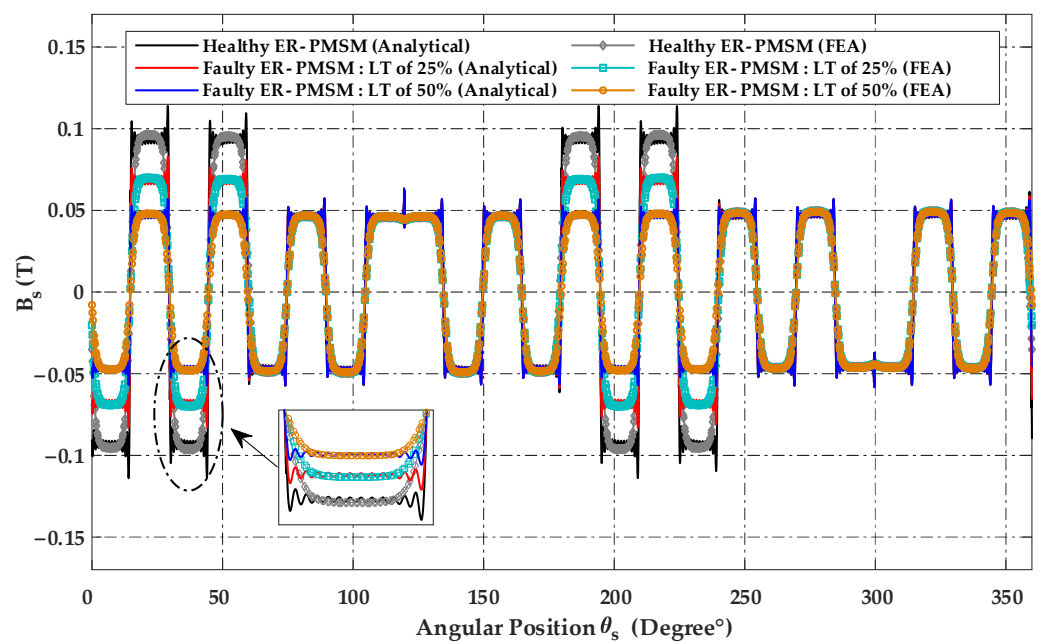


Figure 9. Air-gap flux density distribution in the healthy and faulty cases.

The harmonic spectrum is depicted in Figure 10. The flux density in healthy and faulty circumstances is mainly composed of the fundamental and other harmonics, as well as the appearance of new harmonics attributable to the faults (red arrows). In addition, the amplitude of the fundamental suffers a diminution in the faulty cases compared to the healthy condition.

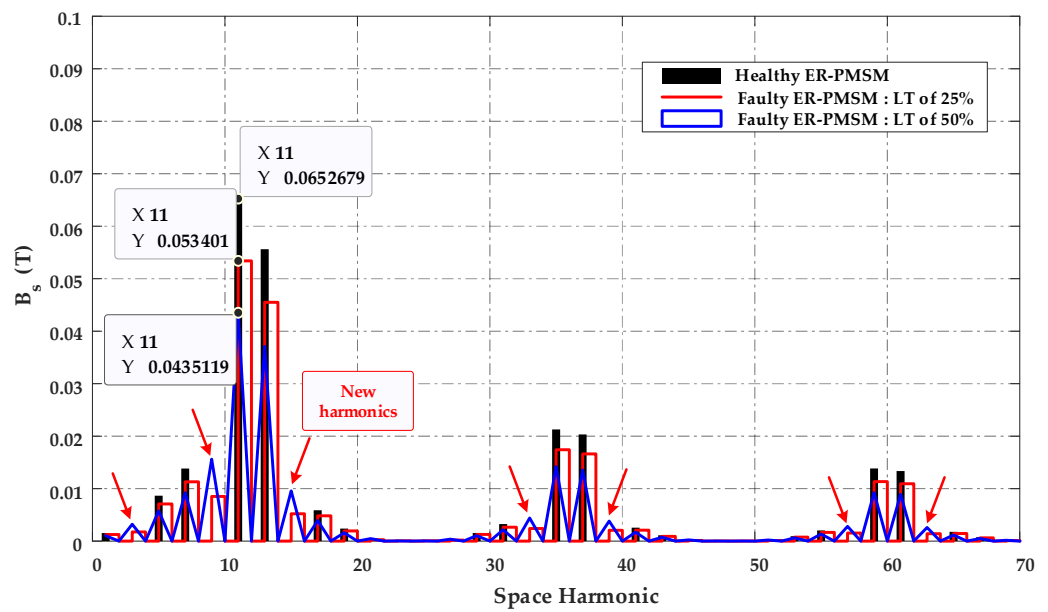


Figure 10. Spatial harmonic spectrum of the healthy and faulty air-gap flux density.

Figure 11 shows the total fluxes generated by the stator power supply in the two situations of the LTs fault of 25% and 50% of phase A, developed theoretically using the analytical model described previously, and the finite element method at a speed of 600 rpm. Due to the change in the stator winding induced by the fault in phase A, an unbalance arises depending on the level of the fault, which leads to torque ripples (Figure 13). This analysis will be used to determine the inductance of the machine in the presence of the fault. The inductances take a critical role in the modeling process, since they consider the many phenomena that might appear within the machine. Accurate modeling will lead to additional information of the signals and a good compromise in terms of the accuracy of the model.

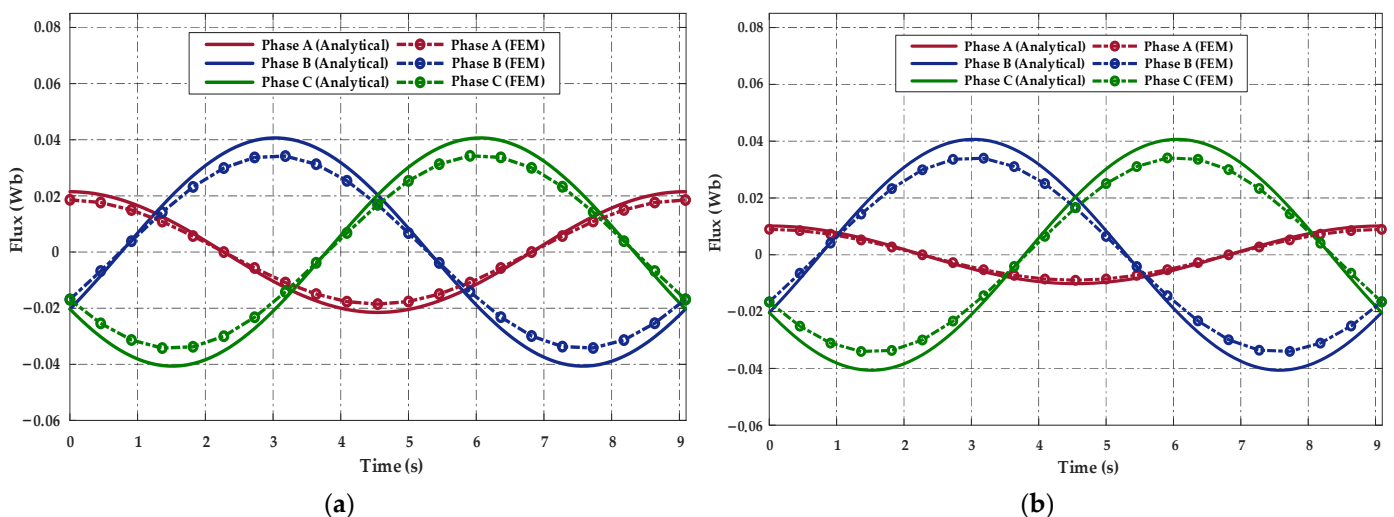
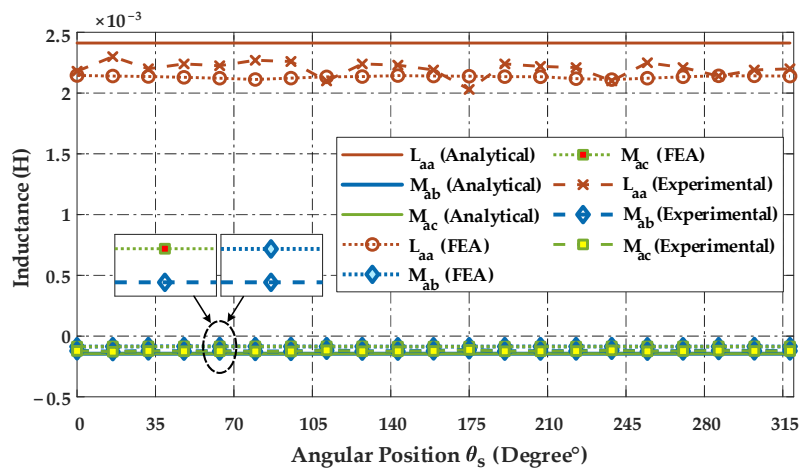


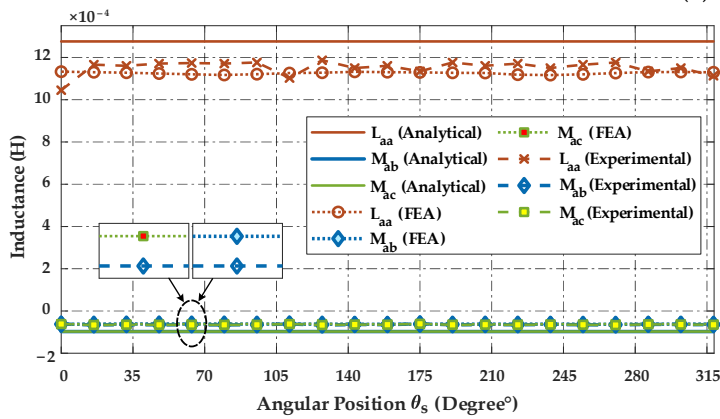
Figure 11. Total flux created by the stator winding, (a) Total flux with 25% of LTs fault; (b) total flux with 50% of LTs fault.

The inductances of the ER-PMSM are reported in Figure 12. The values given for the inductances, calculated using the winding function approach from the real distribution of windings in the stator slots, are closer to those of the finite element analysis and the experimental ones. On the other hand, a considerable discrepancy is noted between the FEA and analytical findings for the analytically calculated inductance. This discrepancy

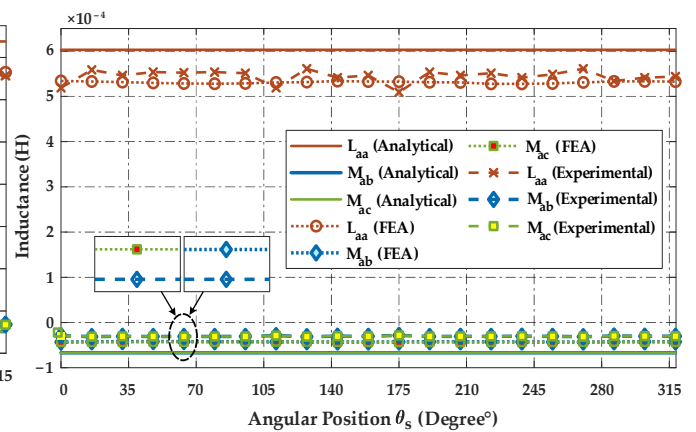
can be associated with the inadequacy of the winding function to take into account the real flux paths, geometry, and nonuniformly saturated iron in an FSCW ER-PMSM machine.



(a)



(b)



(c)

Figure 12. Comparison between inductances derived by the analytical approach, FEA, and experimental measurements. (a) Healthy inductances; (b) faulty inductances with 25% of LTs fault; (c) faulty inductances with 50% of LTs fault.

In Figure 13, the ER-PMSM is operated at nominal load. The temporal representation of the output torque of the machine by FEA for the three cases is provided. In the LTs fault circumstances of 25% and 50% of phase A, the torque decreases accordingly concerning the healthy state, according to the fault’s severity level. Moreover, due to the change of its symmetry, torque ripples appear, which are due to the growth of harmonics. The evolution of the faulty torque reveals torque ripples corresponding to the double of the frequency, owing to the decrease of the resistance and the inductance of a phase, which makes the bandwidth wider. The results concerning the torque are provided in Table 2. It can be observed that the level of the torque ripples is related to the severity of the fault.

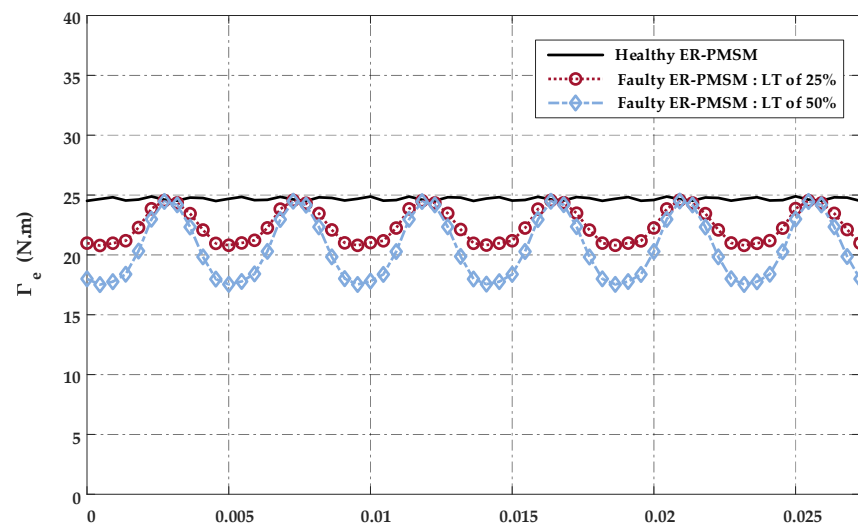


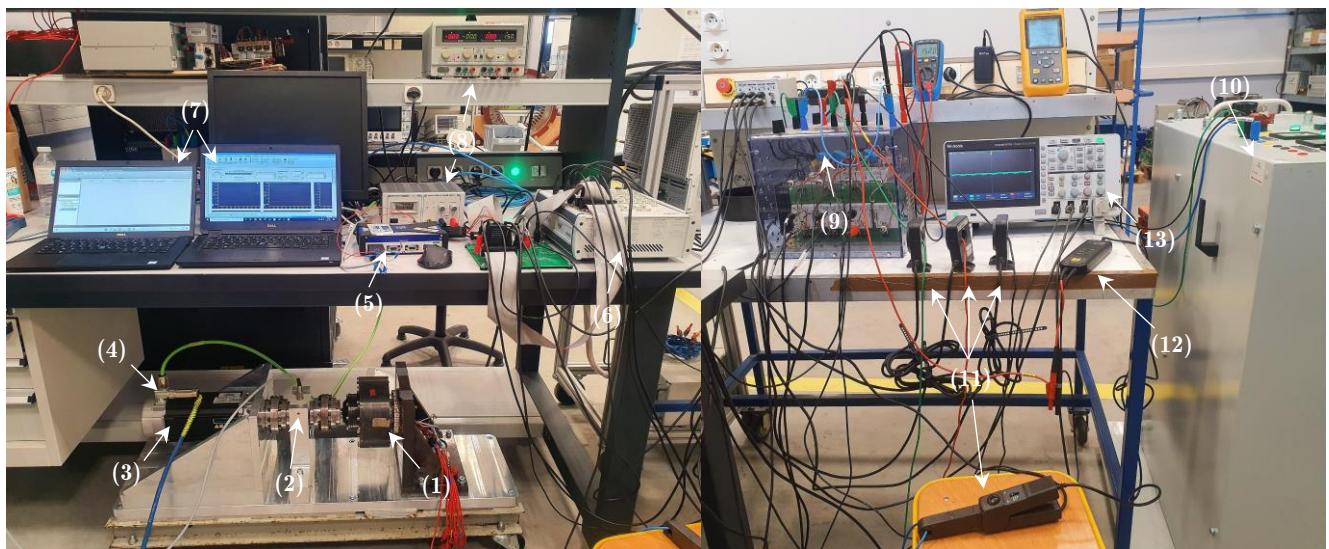
Figure 13. Electromagnetic torque comparison.

Table 2. Summary of simulation results of electromagnetic torque.

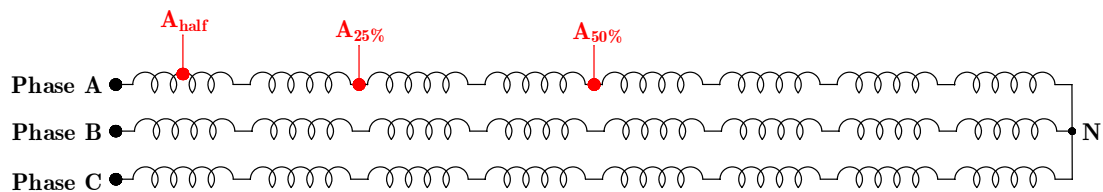
State	Torque Ripples (N.m)
Healthy ER-PMSM	$\begin{cases} \Gamma_{e-\min} = 24.5023 \\ \Gamma_{e-\max} = 24.8956 \end{cases}$
Faulty state: LTs of 25%	$\begin{cases} \Gamma_{e-\min} = 20.7869 \\ \Gamma_{e-\max} = 24.5755 \end{cases}$
Faulty state: LTs of 50%	$\begin{cases} \Gamma_{e-\min} = 17.5335 \\ \Gamma_{e-\max} = 24.4895 \end{cases}$

3. Experimental Setup

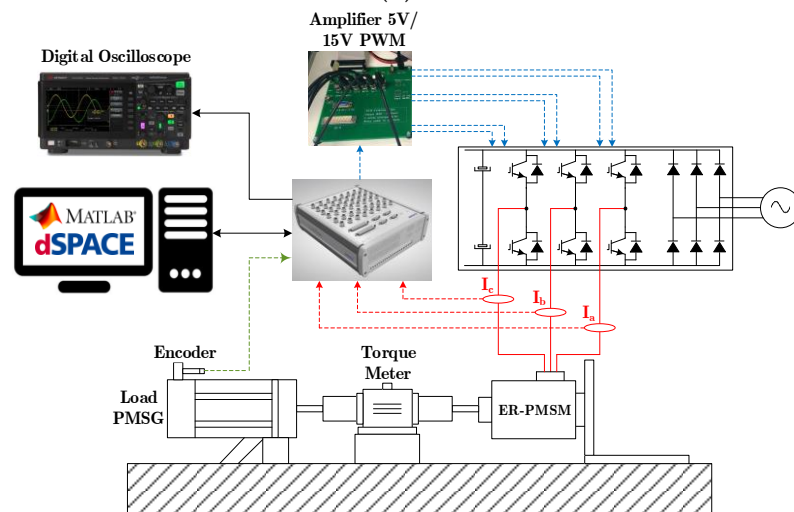
This section describes the configuration and experimental campaign of the test bench devoted to the control and diagnosis of the LTs fault of the ER-PMSM, to validate and verify the theoretical and numerical methodologies. The parameters of the faulty machine are reported in Table 1. The test bench is illustrated in Figure 14a. The structure of the stator winding of the machine has been designed in such a way as to offer the possibility of achieving various levels of LTs and interturn short circuit ITSC defects (Figure 14b). The architecture of the experimental platform is given in Figure 14c. The experimental bench for control and diagnosis consists mainly of a three-phase ER-PMSM of 22 poles and a power of 1.5 kW, coupled to a permanent magnet synchronous generator (PMSG). This PMSG is equipped with an incremental encoder connected to the interface with a specific cable to measure the rotation speed, as well as to capture the exact position of the rotor, whose stator is connected to a three-phase resistive load. The torque is measured via a T22/50 Nm torque meter connected to an MX440B universal amplifier module from HBM's QuantumX. The machine is driven in a closed-loop and the motor is fielded by a Semikron three-phase IGBT inverter at 5 kHz. The control and signal acquisition are performed via a dSpace-MicroLabBox 1202 platform. The DC bus voltage V_{DC} is maintained at 150 V by the grid through the three-phase autotransformer and a diode bridge rectifier.



(a)



(b)



(c)

Figure 14. Experimental setup. (a) Global view of the test bench setup for control and diagnosis of the ER-PMSM; (1) ER-PMSM 1.5 kW; (2) torque meter T22/50 Nm; (3) load PMSG; (4) encoder; (5) MX440B module; (6) dSpace 1202 MicroLabBox; (7) MATLAB/Simulink ControlDesk platform; (8) DC power supply; (9) Semikron 3Φ inverter; (10) power supply 3Φ/50 Hz; (11) current sensors; (12) voltage sensor; (13) digital oscilloscope. (b) Structure of the stator winding of the ER-PMSM; (c) block diagram of the setup.

The faulty harmonics are aimed at kf_s , with the values measured in decibels (dB). As a result, for fault sensitivity, we consider the case of the LTs fault in half of an elementary coil A_{half} , of 25% and 50%, corresponding, respectively, to 11 turns, 44 turns, and 88 turns. In reality, the 25% and 50% cases are rarely possible, and the fault is often apparent on

some turns. Nonetheless, these values, although large, provide a vision of the tendency to monitor the machine with the fault and the evolution of these harmonics.

4. Experimental Results

Figure 14c depicts a synoptic diagram of the experimental implementation that indicates the experimental validation of the ER-PMSM control results in the healthy condition with an LTs fault of 25% and 50%. The experimental results are acquired by a digital oscilloscope linked to the real-time interface. The choice of the sampling frequency significantly impacts the quality of the signals, particularly the phase currents, speeds, and electromagnetic torque, and whatever the control algorithm used. For each healthy/faulty scenario, a load torque condition is tested: 8 Nm for a speed of 600 rpm. In this section, we present the experimental results illustrating the behavior of the ER-PMSM impacted by 25% and 50% LTs fault in its stator winding. Figure 15 depicts the flow chart of the control loop used in this paper with the LTs fault diagnosis.

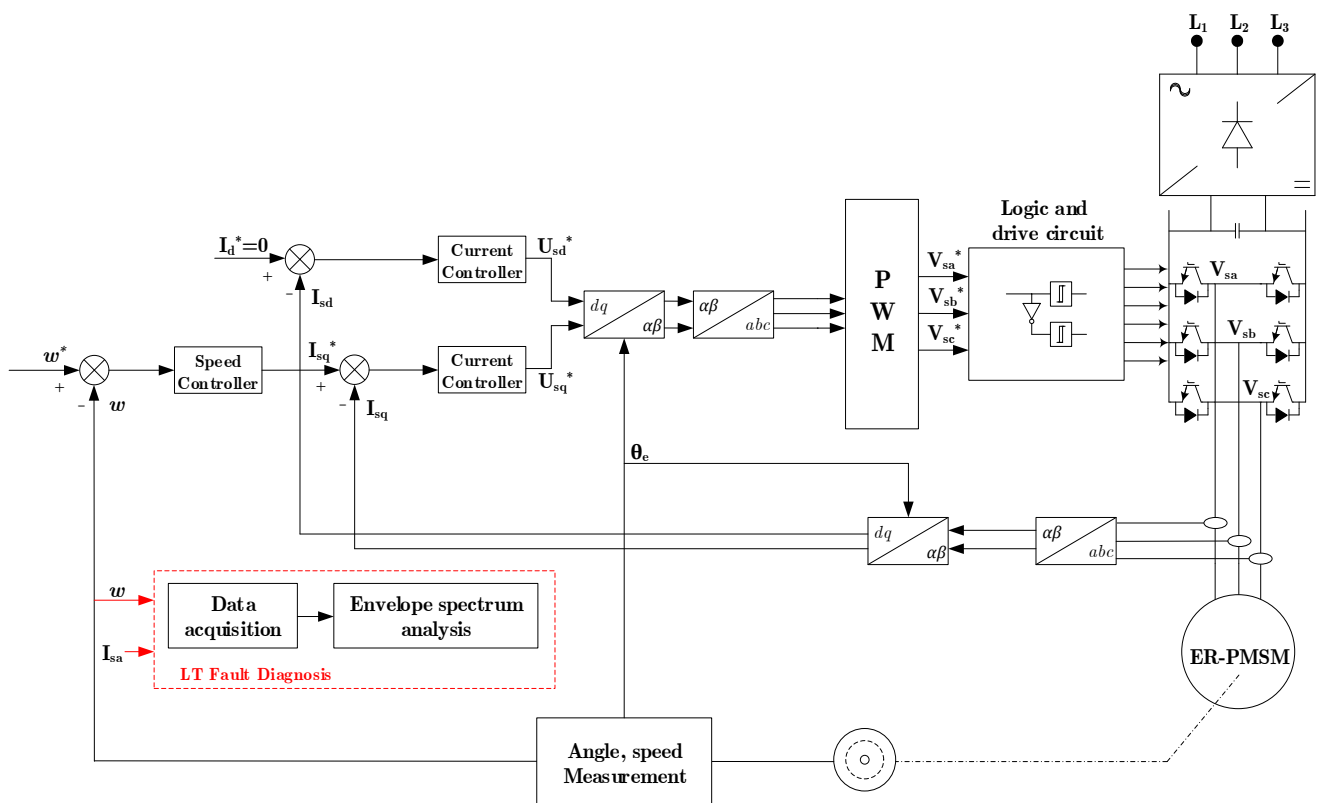


Figure 15. The flow chart of the proposed strategy.

4.1. Healthy State of the ER-PMSM

The following section examines the behavior of the machine in the healthy state. Figure 16 depicts the electrical and mechanical quantities recorded in real-time. The presentation of the experimental results will be restricted to the intersective PWM. We are interested in the rotational speed and the waveform of the stator currents. Figure 16a shows that the rotor speed follows its reference. The three-phase stator currents are shown in Figure 16b and in the d-q rotating frame in Figure 16c. The spectral analysis of the signals offers a way to diagnose this type of stator winding fault. We present the spectral analysis of the rotational speed and the stator current, using the fast Fourier transform (FFT) in steady state at rated load. We will show how this method makes it possible to determine the frequency content of the rotational speed and the stator current, and thus to find the lines associated with the LTs faults of 25% and 50%.

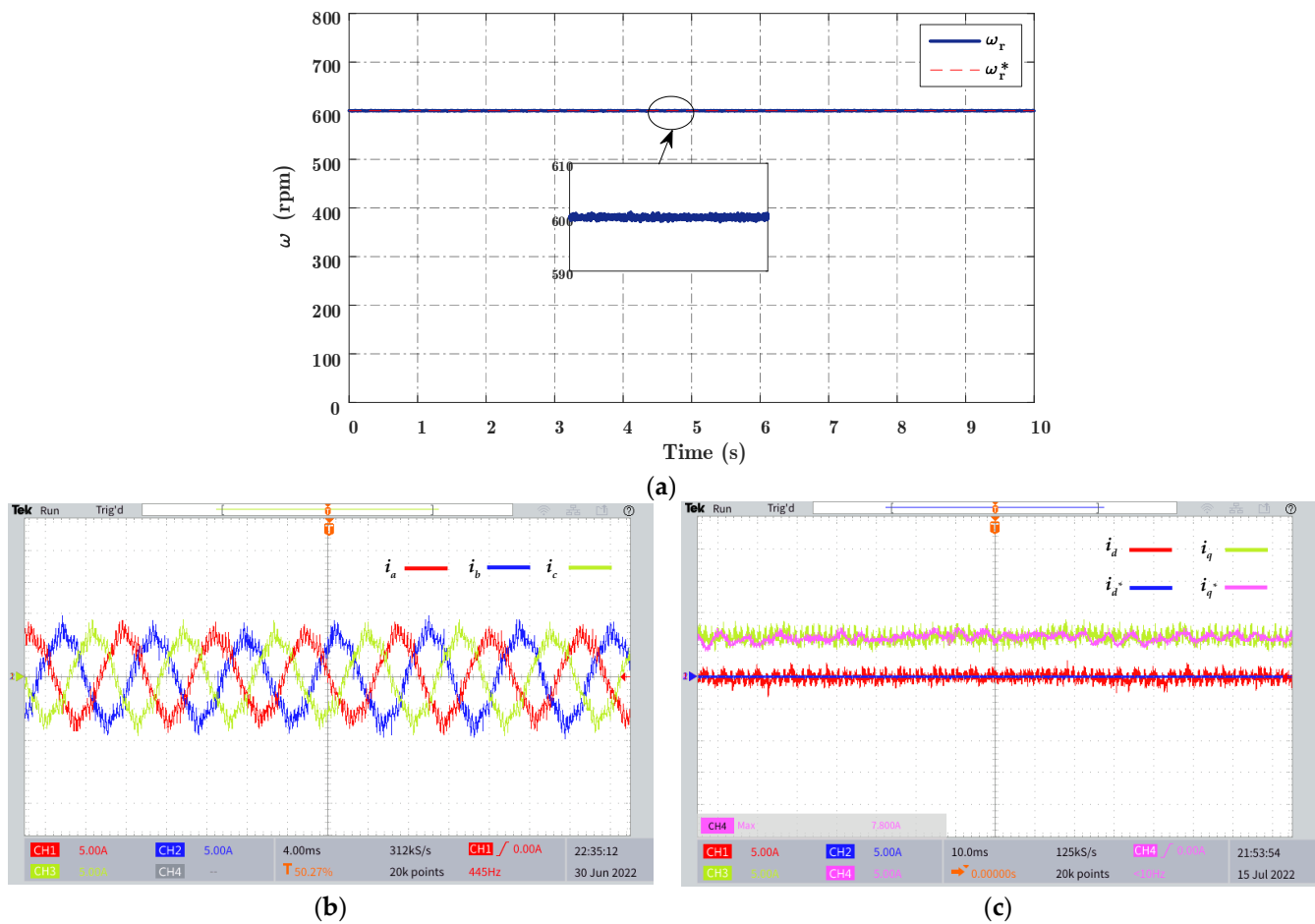


Figure 16. Electrical and mechanical characteristics in the healthy state. (a) Rotor speed; (b) stator phase currents; (c) direct and quadratic current component.

4.2. Faulty State of the ER-PMSM

The following section provides the experimental results of the machine with the LTs fault. Figures 17 and 18 exhibit the results obtained from the control of the different electrical and mechanical parameters of the machine with a fault in the stator winding. The presence of the LTs fault in stator phase A, according to the severity level, shows:

- The rotor speed is not substantially influenced by the LTs fault because of the control loop that hides and compensates for the effect of the fault;
- High ripples arise in the stator current of phase A, the direct current i_d , and the quadratic current i_q . The influence of the fault generates an unbalance and a noticeable variation in the current envelope.

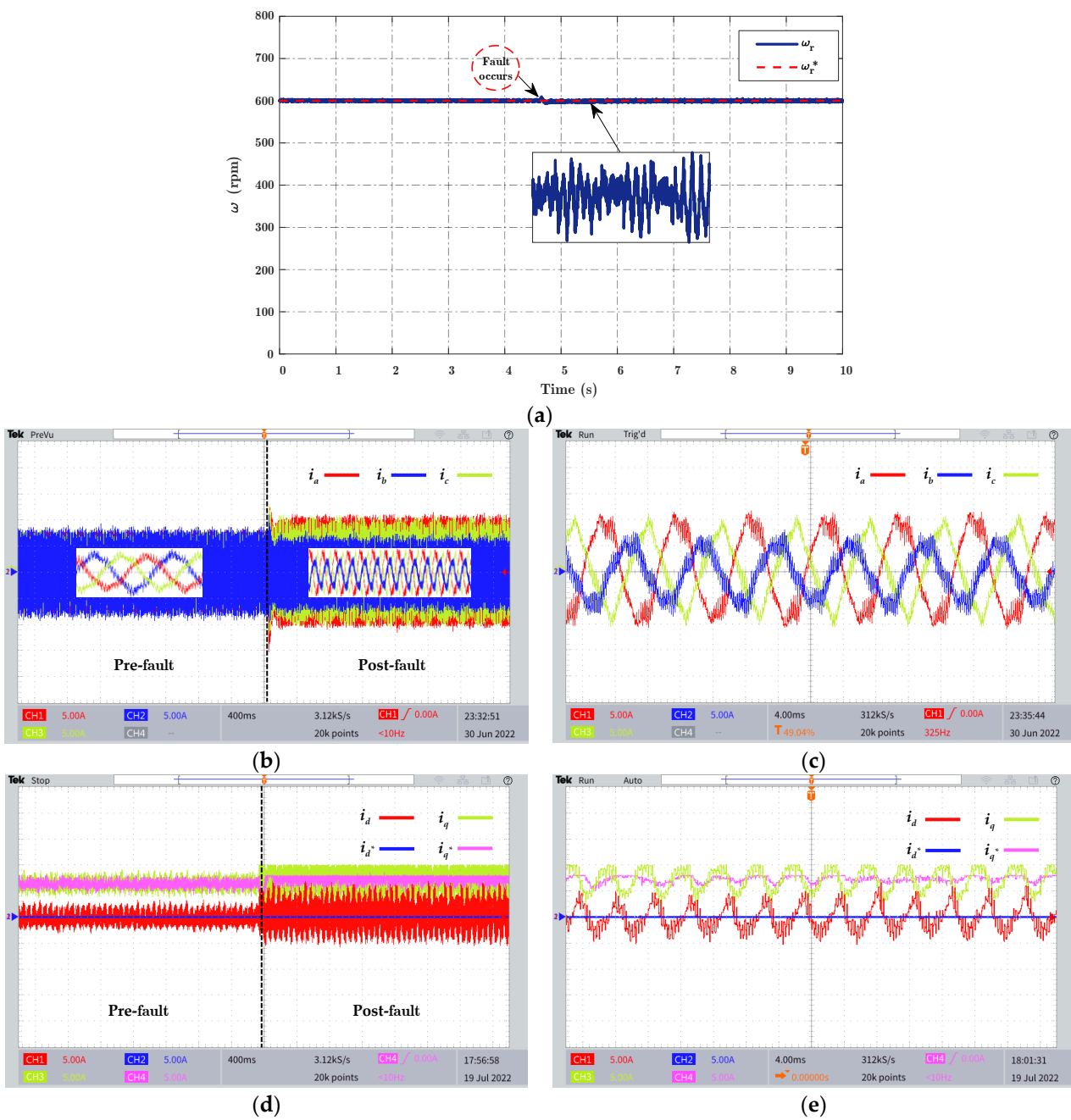


Figure 17. Electrical and mechanical characteristics in the faulty state with an LTs fault of 25%. (a) Rotor speed; (b) stator phase currents; (c) zoom of the stator phase currents; (d) direct and quadratic current component; (e) zoom of the direct and quadratic current component.

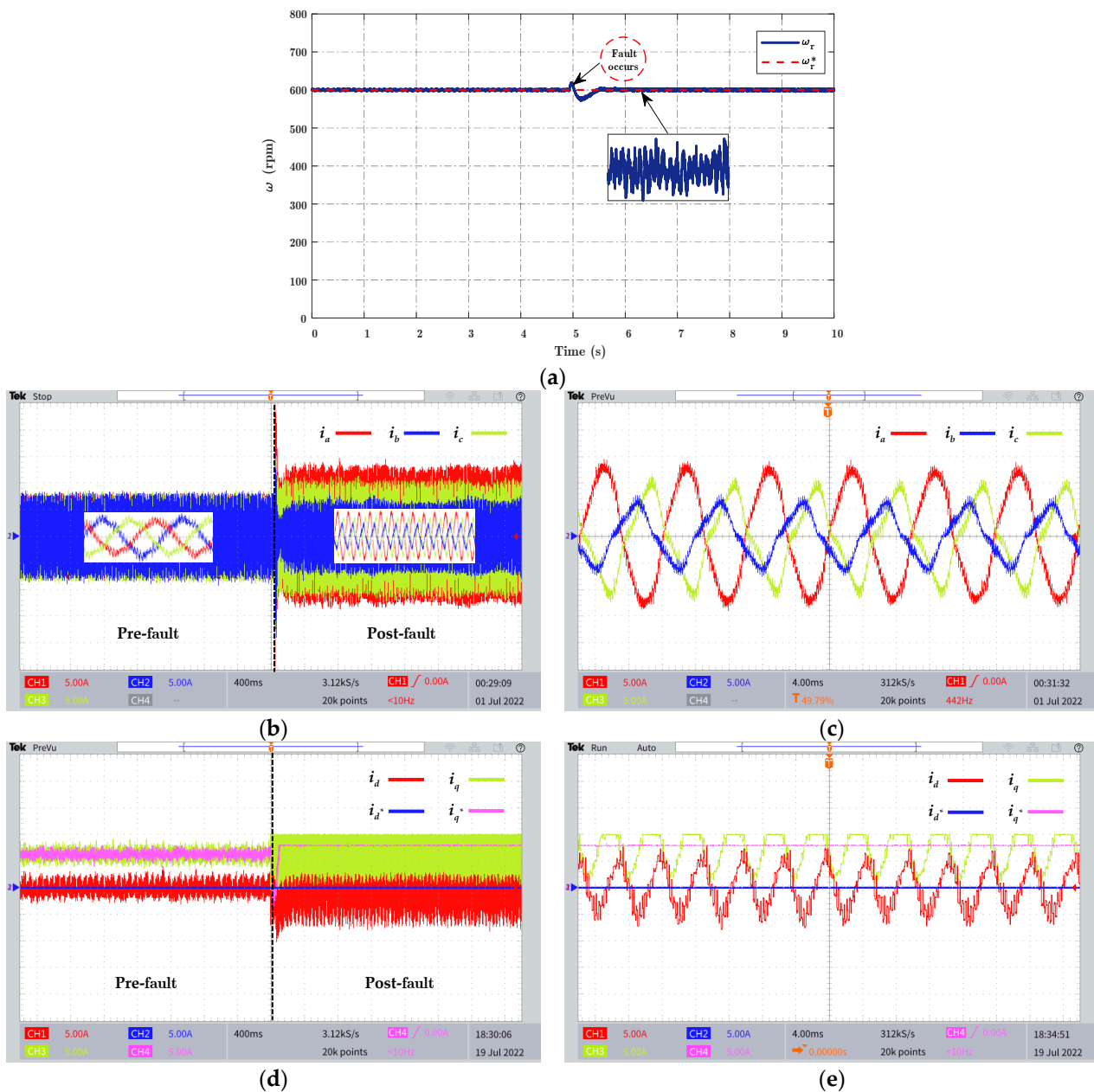


Figure 18. Electrical and mechanical characteristics in the faulty state with an LTs fault of 50%. (a) Rotor speed; (b) stator phase currents; (c) zoom of the stator phase currents; (d) direct and quadratic current component; (e) zoom of the direct and quadratic current component.

4.2.1. Motor Speed Signature Analysis

The examination of the motor speed signature analysis (MSSA) may provide a non-invasive method applied for the detection of stator winding faults. It is a nonparametric approach devoted to the analysis of stationary phenomena [31,32]. Figure 19 illustrates the spectrum analysis of the speed in the presence of an LTs fault of 25% to 50%. According to this study, we notice the appearance or the presence of several components having a direct relation with the defect according to the specified degree of severity. The appearance of the lines is an indicator of the existence of the LTs fault.

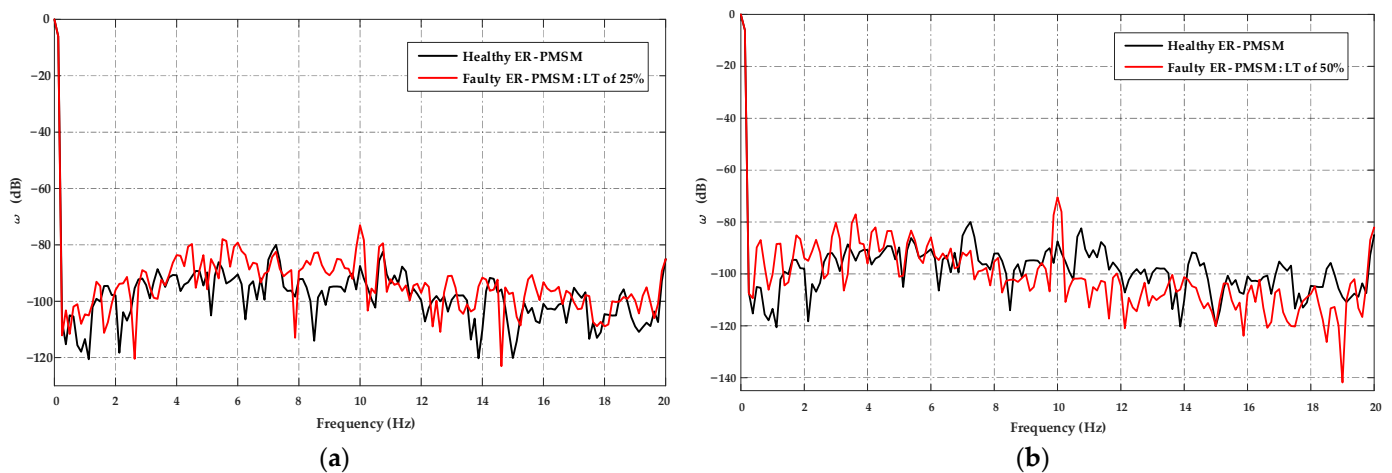


Figure 19. Experimental speed spectrum of the ER-PMSM at 8 Nm load and 600 rpm, in healthy and faulty conditions. (a) LTs fault of 25%; (b) LTs fault of 50%.

4.2.2. Motor Current Signature Analysis

The next stage is to evaluate the application of the spectral analysis of the stator phase current envelope signal to LTs detection. The steady-state stator phase current envelope spectra for the motor operating with $f_s = 110$ Hz at 8 Nm load for 25% LTs fault level is illustrated in Figure 20. The examination of the motor current signature analysis (MCSA) reveals the influence of the LTs fault in the appearance of harmonics around the fundamental, which increases with the fault intensity. The influence of the fault is manifested by the presence of new visible frequency components in the current spectrum around the fundamental at $2f_s$ and $3f_s$. Based on this analysis, it can be inferred that the rise in amplitudes induced by the fault is significant. We can also highlight more typical criteria, such as the occurrence of kf_s frequency lines near the fundamental ($k = 1, 2, 3, 4 \dots$) on the stator current spectrum. Table 3 illustrates the magnitudes and frequency of the ER-PMSM stator current analysis fault.

Table 3. Experimental magnitude of current components generated by the ER-PMSM at 8 Nm load and $f_s = 110$ Hz.

ER-PMSM Magnitude (dB)	Current (dB)				
	$f_s = 110$ Hz	$2f_s = 220$ Hz	$3f_s = 330$ Hz	$4f_s = 440$ Hz	$5f_s = 550$ Hz
Healthy state	0	−43.361	−41.096	−55.616	−23.937
Faulty state: LTs of A_{half}	0	−43.177	−35.001	−45.819	−22.828
Faulty state: LTs of 25%	0	−31.636	−20.759	−38.989	−21.159
Faulty state: LTs of 50%	0	−37.708	−20.689	−42.237	−31.881

According to Figure 20, we notice that after the presence of the fault at a level of 25%, an appearance and increase of harmonics is reflected in the frequency domain. The presence of the LTs fault causes torque and speed ripples, which leads to significant mechanical vibrations in the machine, as well as an unbalance that manifests itself in the form of an important increase in the current of the faulty phase and a less significant increase for the other two phases. The spectral analysis of the MCSA indicates a visible rise in amplitude at $2f_s$, $3f_s$, and $4f_s$ for both fault levels. However, the fifth harmonic of the spectrum (550 Hz) will not be influenced by the 50% LTs fault. According to these results, we observe the existence of proportionality between the severity level of the LTs fault and the amplitude of the characteristic harmonic of the fault. Therefore, we can subsequently detect an incipient fault, which is the main objective of the LTs fault diagnosis. All information acquired from

the spectrum analysis can be employed in an automated fault detection process, while analyzing the presence of new harmonics and setting detection thresholds using adaptive observers for reconfiguration and fault isolation.

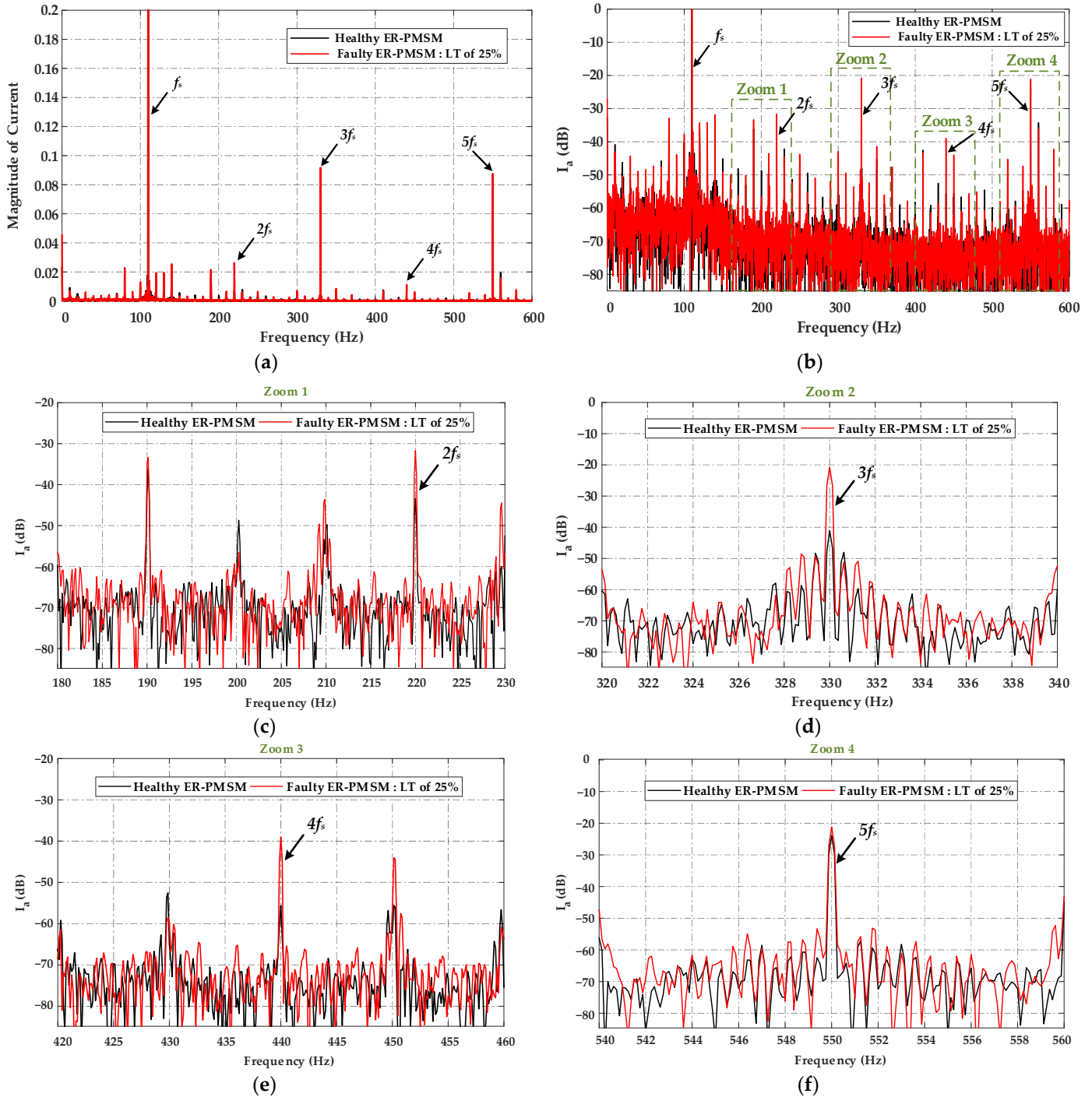


Figure 20. (a–f) Experimental current spectrum of the ER-PMSM at 8 Nm load and 600 rpm, in healthy and faulty conditions with an LTs fault of 25%.

The validity of the analytical model was proven by two approaches: FEA and experimental measurement of inductances and electromotive forces of the healthy and faulty machines. The occurrence of new harmonics can be attributed to several factors connected to the LTs fault, including torque and speed ripples, system nonlinearity, and unbalance of the ER-PMSM electromotive force. These factors can induce variations in the electri-

cal and mechanical behavior of the machine, resulting in spectral alterations that can be detected and analyzed to diagnose the fault. While validation of the analytical model by FEA and experimental measurements is crucial, understanding the underlying reasons for the spectrum changes is equally important for effective fault diagnosis in real-world applications.

5. Conclusions

This paper presents a new approach for modeling lack of turns (LTs) faults in the stator winding of external rotor permanent magnet synchronous motors (ER-PMSMs), which are of major importance in permanent magnet (PM) electrical machines since, in rotation, the induction effect generated by PMs aggravates the effects of these faults. Different operating conditions of ER-PMSMs with LTs fault provide a reference for real-time diagnosis, prediction, and maintenance planning. The suggested method has substantial advantages, such as fast calculation, good precision, and explicit physical correlations between different factors. For this purpose, theoretical operational performances of various operating situations have been evaluated.

The paper also examines the problem of diagnosing LTs faults in ER-PMSMs at their early stage by analyzing the spectral content of the speed and current signatures under various operating situations. The provided results confirm the efficiency of the diagnosis and the application of spectral analysis for the extraction of LTs fault indicators.

Future research will focus on the development and combination of adaptive fault-tolerant control of LTs faults, advanced fault diagnosis methodologies for ER-PMSMs, and the implementation of automated fault detection processes in automotive applications.

Author Contributions: Conceptualization, A.B., R.R., R.P., and D.B.; methodology, A.B., R.R., and R.P.; software, A.B.; validation, R.R., R.P., D.B., and Y.Z.; formal analysis, A.B.; investigation, A.B.; resources, A.B.; data curation, A.B.; experimental measurements, A.B.; writing—original draft preparation, A.B.; writing—review and editing, A.B., R.R., R.P., and D.B.; visualization, A.B., R.P., Y.Z., D.B., and R.R.; supervision, R.R., D.B., R.P., and Y.Z.; project administration, R.R., D.B., R.P., and Y.Z.; funding acquisition, R.R., and R.P. All authors have read and agreed to the published version of the manuscript.

Funding: This research work received no external funding.

Data Availability Statement: Data sharing not applicable.

Conflicts of Interest: The authors declare no conflict of interest.

References

1. Łebkowski, A. Design, Analysis of the Location and Materials of Neodymium Magnets on the Torque and Power of in-Wheel External Rotor PMSM for Electric Vehicles. *Energies* **2018**, *11*, 2293. [\[CrossRef\]](#)
2. Pop, C.V.; Fodorean, D.; Husar, C.; Irimia, C. Structural Behavior Evaluation of an In-Wheel Motor Based on Numerical and Experimental Approach. *Electr. Eng.* **2020**, *102*, 65–74. [\[CrossRef\]](#)
3. Ma, C.; Gao, Y.; Degano, M.; Wang, Y.; Fang, J.; Gerada, C.; Zhou, S.; Mu, Y. Eccentric Position Diagnosis of Static Eccentricity Fault of External Rotor Permanent Magnet Synchronous Motor as an In-wheel Motor. *IET Electr. Power Appl.* **2020**, *14*, 2263–2272. [\[CrossRef\]](#)
4. Ebrahimi, S.H.; Choux, M.; Huynh, V.K. Real-Time Detection of Incipient Inter-Turn Short Circuit and Sensor Faults in Permanent Magnet Synchronous Motor Drives Based on Generalized Likelihood Ratio Test and Structural Analysis. *Sensors* **2022**, *22*, 3407. [\[CrossRef\]](#) [\[PubMed\]](#)
5. Ebrahimi, B.M.; Javan Roshtkhari, M.; Faiz, J.; Khatami, S.V. Advanced Eccentricity Fault Recognition in Permanent Magnet Synchronous Motors Using Stator Current Signature Analysis. *IEEE Trans. Ind. Electron.* **2014**, *61*, 2041–2052. [\[CrossRef\]](#)
6. Belkhadir, A.; Belkhat, D.; Zidani, Y.; Pusca, R.; Romary, R. Torque Ripple Minimization Control of Permanent Magnet Synchronous Motor Using Adaptive Ant Colony Optimization. In Proceedings of the 2022 8th International Conference on Control, Decision and Information Technologies (CoDIT), Istanbul, Turkey, 17–20 May 2022; pp. 629–635.
7. Orłowska-Kowalska, T.; Wolkiewicz, M.; Pietrzak, P.; Skowron, M.; Ewert, P.; Tarchala, G.; Krzysztofiak, M.; Kowalski, C.T. Fault Diagnosis and Fault-Tolerant Control of PMSM Drives—State of the Art and Future Challenges. *IEEE Access* **2022**, *10*, 59979–60024. [\[CrossRef\]](#)

8. Kudelina, K.; Asad, B.; Vaimann, T.; Rassõlkin, A.; Kallaste, A.; Khang, H. Van Methods of Condition Monitoring and Fault Detection for Electrical Machines. *Energies* **2021**, *14*, 7459. [[CrossRef](#)]
9. Ullah, Z.; Hur, J. A Comprehensive Review of Winding Short Circuit Fault and Irreversible Demagnetization Fault Detection in PM Type Machines. *Energies* **2018**, *11*, 3309. [[CrossRef](#)]
10. Chen, Y.; Liang, S.; Li, W.; Liang, H.; Wang, C. Faults and Diagnosis Methods of Permanent Magnet Synchronous Motors: A Review. *Appl. Sci.* **2019**, *9*, 2116. [[CrossRef](#)]
11. Solís, R.; Torres, L.; Pérez, P. Review of Methods for Diagnosing Faults in the Stators of BLDC Motors. *Processes* **2022**, *11*, 82. [[CrossRef](#)]
12. Liang, H.; Chen, Y.; Liang, S.; Wang, C. Fault Detection of Stator Inter-Turn Short-Circuit in PMSM on Stator Current and Vibration Signal. *Appl. Sci.* **2018**, *8*, 1677. [[CrossRef](#)]
13. Hang, J.; Zhang, J.; Cheng, M.; Huang, J. Online Interturn Fault Diagnosis of Permanent Magnet Synchronous Machine Using Zero-Sequence Components. *IEEE Trans. Power Electron.* **2015**, *30*, 6731–6741. [[CrossRef](#)]
14. Yepes, A.G.; Fonseca, D.S.B.; Antunes, H.R.P.; Lopez, O.; Marques Cardoso, A.J.; Doval-Gandoy, J. Discrimination Between Eccentricity and Interturn Faults Using Current or Voltage-Reference Signature Analysis in Symmetrical Six-Phase Induction Machines. *IEEE Trans. Power Electron.* **2023**, *38*, 2421–2434. [[CrossRef](#)]
15. Yang, M.; Chai, N.; Liu, Z.; Ren, B.; Xu, D. Motor Speed Signature Analysis for Local Bearing Fault Detection with Noise Cancellation Based on Improved Drive Algorithm. *IEEE Trans. Ind. Electron.* **2020**, *67*, 4172–4182. [[CrossRef](#)]
16. Haje Obeid, N.; Battiston, A.; Boileau, T.; Nahid-Mobarakeh, B. Early Intermittent Interturn Fault Detection and Localization for a Permanent Magnet Synchronous Motor of Electrical Vehicles Using Wavelet Transform. *IEEE Trans. Transp. Electrification* **2017**, *3*, 694–702. [[CrossRef](#)]
17. Espinosa, A.G.; Rosero, J.A.; Cusido, J.; Romeral, L.; Ortega, J.A. Fault Detection by Means of Hilbert–Huang Transform of the Stator Current in a PMSM With Demagnetization. *IEEE Trans. Energy Convers.* **2010**, *25*, 312–318. [[CrossRef](#)]
18. Pusca, R.; Romary, R.; Touti, E.; Livinti, P.; Nuca, I.; Ceban, A. Procedure for Detection of Stator Inter-Turn Short Circuit in AC Machines Measuring the External Magnetic Field. *Energies* **2021**, *14*, 1132. [[CrossRef](#)]
19. Irhoumah, M.; Pusca, R.; Lefèvre, E.; Mercier, D.; Romary, R. Stray Flux Multi-Sensor for Stator Fault Detection in Synchronous Machines. *Electronics* **2021**, *10*, 2313. [[CrossRef](#)]
20. Irhoumah, M.; Pusca, R.; Lefevre, E.; Mercier, D.; Romary, R.; Demian, C. Information Fusion with Belief Functions for Detection of Interturn Short-Circuit Faults in Electrical Machines Using External Flux Sensors. *IEEE Trans. Ind. Electron.* **2018**, *65*, 2642–2652. [[CrossRef](#)]
21. Irhoumah, M.; Pusca, R.; Lefevre, E.; Mercier, D.; Romary, R. Detection of the Stator Winding Inter-Turn Faults in Asynchronous and Synchronous Machines Through the Correlation Between Harmonics of the Voltage of Two Magnetic Flux Sensors. *IEEE Trans. Ind. Appl.* **2019**, *55*, 2682–2689. [[CrossRef](#)]
22. Shih, K.-J.; Hsieh, M.-F.; Chen, B.-J.; Huang, S.-F. Machine Learning for Inter-Turn Short-Circuit Fault Diagnosis in Permanent Magnet Synchronous Motors. *IEEE Trans. Magn.* **2022**, *58*, 1–7. [[CrossRef](#)]
23. Pietrzak, P.; Wolkiewicz, M.; Orłowska-Kowalska, T. PMSM Stator Winding Fault Detection and Classification Based on Bispectrum Analysis and Convolutional Neural Network. *IEEE Trans. Ind. Electron.* **2023**, *70*, 5192–5202. [[CrossRef](#)]
24. Farshadnia, M. *Advanced Theory of Fractional-Slot Concentrated- Wound Permanent Magnet Synchronous Machines*; Springer: Berlin/Heidelberg, Germany, 2018; ISBN 978-981-10-8708-0.
25. Pyrhonen, J. Juha Pyrhönen, Tapani Jokinen, Valéria Hrabovcová. In *Design of Rotating Electrical Machines*; Wiley: Hoboken, NJ, USA, 2014; Volume 614, ISBN 9781118581575.
26. Bianchi, N.; Fornasiero, E. Impact of MMF Space Harmonic on Rotor Losses in Fractional-Slot Permanent-Magnet Machines. *IEEE Trans. Energy Convers.* **2009**, *24*, 323–328. [[CrossRef](#)]
27. EL-Refaie, A.M. Fractional-Slot Concentrated-Windings Synchronous Permanent Magnet Machines: Opportunities and Challenges. *IEEE Trans. Ind. Electron.* **2010**, *57*, 107–121. [[CrossRef](#)]
28. Di Tommaso, A.O.; Genduso, F.; Miceli, R. A Software for the Evaluation of Winding Factor Harmonic Distribution in High Efficiency Electrical Motors and Generators. In Proceedings of the 2013 8th Eighth International Conference and Exhibition on Ecological Vehicles and Renewable Energies (EVER), Monte Carlo, Monaco, 27–30 March 2013. [[CrossRef](#)]
29. Hamiti, T.; Lubin, T.; Baghli, L.; Rezzoug, A. Modeling of a Synchronous Reluctance Machine Accounting for Space Harmonics in View of Torque Ripple Minimization. *Math. Comput. Simul.* **2010**, *81*, 354–366. [[CrossRef](#)]
30. *IEEE Std 115a*; IEEE Standard Procedures for Obtaining Synchronous Machine Parameters by Standstill Frequency Response Testing. IEEE: Piscataway, NJ, USA, 1987.
31. Shi, P.; Chen, Z.; Vagapov, Y.; Zouaoui, Z. A New Diagnosis of Broken Rotor Bar Fault Extent in Three Phase Squirrel Cage Induction Motor. *Mech. Syst. Signal Process.* **2014**, *42*, 388–403. [[CrossRef](#)]
32. Moumene, I.; Ouelaa, N. Application of the Wavelets Multiresolution Analysis and the High-Frequency Resonance Technique for Gears and Bearings Faults Diagnosis. *Int. J. Adv. Manuf. Technol.* **2016**, *83*, 1315–1339. [[CrossRef](#)]

Disclaimer/Publisher’s Note: The statements, opinions and data contained in all publications are solely those of the individual author(s) and contributor(s) and not of MDPI and/or the editor(s). MDPI and/or the editor(s) disclaim responsibility for any injury to people or property resulting from any ideas, methods, instructions or products referred to in the content.